GEOPHYSICS, VOL. 76, NO. 1 (JANUARY-FEBRUARY 2011); P. S1–S13, 19 FIGS.
10.1190/1.3511352

OFFICIAL ONLINE VERSION: http://link.aip.org/link/?GPY/76/S1

Full-azimuth subsurface angle domain wavefield decomposition and imaging Part I: Directional and reflection image gathers

Zvi Koren[1] and Igor Ravve[1]

ABSTRACT

We present a new subsurface angle-domain seismic imaging system for generating and extracting high-resolution information about subsurface angle-dependent reflectivity. The system enables geophysicists to use all recorded seismic data in a continuous fashion directly in the subsurface local angle domain (LAD), resulting in two complementary, full-azimuth, common-image-angle gather systems: directional and reflection. The complete set of information from both types of angle gathers leads to accurate, high-resolution, reliable velocity model determination and reservoir characterization. The directional angle decomposition enables the implementation of specular and diffraction imaging in real 3D isotropic/anisotropic geological models, leading to simultaneous emphasis on continuous structural surfaces and discontinuous objects such as faults and small-scale fractures. Structural attributes at each subsurface point, e.g., dip, azimuth and continuity, can be derived directly from the directional angle gathers. The reflection-angle gathers display reflectivity as a function of the opening angle and opening azimuth. These gathers are most meaningful in the vicinity of actual local reflecting surfaces, where the reflection angles are measured with respect to the derived background specular direction. The reflection-angle gathers are used for automatic picking of full-azimuth angle-domain residual moveouts (RMO) which, together with the derived background orientations of the subsurface reflection horizons, provide a complete set of input data to isotropic/anisotropic tomography. The full-azimuth, angle-dependent amplitude variations are used for reliable and accurate amplitude versus angle and azimuth (AVAZ) analysis and reservoir characterization. The proposed system is most effective for imaging and analysis below complex structures, such as subsalt and subbasalt, high-velocity carbonate rocks, shallow low-velocity gas pockets, and others. In addition, it enables accurate azimuthal anisotropic imaging and analysis, providing optimal solutions for fracture detection and reservoir characterization.

INTRODUCTION

The theory and implementation of so-called true amplitude, ray-based angle-domain imaging have been intensively studied using the Kirchhoff integral and the Born modeling/inversion formula. Kirchhoff-type migrations invert for the plane-wave reflection coefficient free of geometrical spreading, assuming the reflection occurs along smooth and continuous interfaces (Bleistein, 1987; Goldin, 1992; Schleicher et al., 1993; Hubral et al., 1996; Tygel et al., 1996; Schleicher et al., 2007). Born-type migrations/inversions are based on linearized single scattering of the wavefield within a known smooth background velocity model. This idea was introduced by Beylkin (1985) and Miller et al. (1987) for acoustic migration using the generalized Radon transform (GRT) and its inverse, and Beylkin and Burridge (1990) extended the theory for isotropic elastic models. A numerical analysis for the implementation of the inverse GRT with an efficient discretization scheme was proposed by de Hoop and Spencer (1996). De Hoop and Bleistein (1997) and de Hoop et al. (1999) extended the GRT derivation to handle anisotropic models containing either point scatterers or smooth interfaces.

Many papers have been published which study and emphasize the importance of generating common-image-angle gathers directly at the subsurface points rather than the universally used surface-offset image gathers, especially in complex geological areas where the wavefield includes multipathing (e.g., ten Kroode et al., 1994; Nolan and Symes, 1996; Brandsberg-Dahl et al., 1999; Rousseau et al., 2000; Xu et al., 2001; Audebert et al., 2002; Koren et al., 2002; Rickett and Sava, 2002; Brandsberg-Dahl et al., 2003; Foss and Ursin, 2004; Sollid and Ursin, 2003; Soubaras, 2003; Bleistein et al., 2005a, 2005b; Wu and Chen, 2006; Biondi, 2007a, 2007b).

Manuscript received by the Editor 28 December 2009; revised manuscript received 13 July 2010; published online 4 January 2011.
[1]Paradigm Geophysical, Herzliya, Israel. E-mail: zvi.koren@pdgm.com; igor.ravve@pdgm.com, iravve@hotmail.com.

Although the theory of angle-domain imaging is well established, its implementation, especially for large-scale 3D models or for high-resolution reservoir imaging, remains extremely challenging. A numerical implementation of a GRT type of true amplitude ray-based angle-domain migration in real 3D complex geological areas, entitled common reflection-angle migration (CRAM), has been presented by Koren et al. (2002). Unlike conventional ray-based imaging methods, ray tracing is performed from the image points up to the surface where one-way "diffracted" rays are traced in all directions (including turning rays), forming a system of ray pairs for mapping (binning) the recorded surface seismic data into reflection-angle gathers. A similar approach has been proposed in Brandsberg-Dahl et al. (2003) and Sollid and Ursin (2003).

This paper presents an extension of CRAM, where the imaged data events are decomposed in the local angle domain (LAD) (or GRT domain), into two complementary full-azimuth angle gathers: directional and reflection (Koren et al., 2007, and Koren et al., 2008). The combination of the two angle gathers, together with the ability to handle the full-azimuth information in a continuous manner, comprises a much improved method for subsurface angle-domain seismic imaging that enables the generation and extraction of high-resolution information about subsurface angle-dependent reflectivity. The complete set of information from both angle gather types allows us to distinguish between continuous structural surfaces and discontinuous objects, such as faults and small-scale fractures, leading to more accurate, high-resolution, high-certainty velocity model determination and reservoir characterization.

Part I of this paper is organized as follows: The first section, "Method," provides the main principles and motivations for generating the two complementary angle gathers, emphasizing the new level of information that can be obtained using its applications. The second section, "Full-azimuth subsurface angle-domain decomposition: directional and reflection gathers," provides the mathematical details used to generate the proposed angle gathers, and describes the construction of the new 3D cylindrical gathers. Real data examples, land and marine, are presented in the "Field examples" section. These examples demonstrate the strength of the different types of weighted energy stacks using directional angle gathers, and present the rich information that can be obtained from the full-azimuth reflection-angle gathers for kinematic and dynamic analysis. In the final section of the paper, we present our "Conclusions." In Part II of this work we define the local angle domain (LAD) components and derive transformations from the incident and scattered slowness vectors to the LAD angles and vice versa, for general anisotropic media and converted waves.

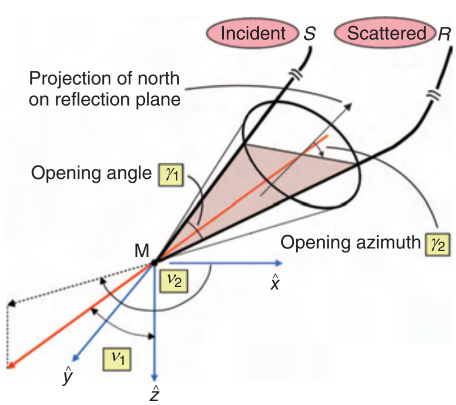

Figure 1. Example of a selected ray pair (incident and scattered) at a given subsurface point **M** and the four angles associated with the LAD: dip ν_1 and azimuth ν_2 of the ray pair normal, opening angle γ_1 and opening azimuth γ_2. Four scalar angles describing the directions of the incident and reflected rays could be related to four LAD angles, and vice versa.

METHOD

The proposed method follows the concept of imaging and analysis in the local angle domain (LAD) in isotropy/anisotropy subsurface models. Imaging systems involve the interaction of two wavefields at the image points: incident and scattered (reflected/diffracted). Each wavefield can be decomposed into local plane waves (or rays), indicating the direction of propagation. The direction of the incident and scattered rays can be described conventionally by their respective polar angles. Each polar angle includes two components — dip and azimuth. Note that throughout the paper, the term ray direction refers to the direction of its slowness (or phase velocity). The imaging stage involves combining a huge number of ray pairs representing the incident and scattered rays. Each ray pair maps the seismic data recorded on the acquisition surface into the 4D LAD space. In our notation, these angles are dip ν_1 and azimuth ν_2 of the ray pair normal, opening angle γ_1 and opening azimuth γ_2, as shown in Figure 1. Four scalar angles describing the directions of the incident and scattered rays could be related to four LAD angles, and vice versa. They are mapped as forward and inverse LAD transforms, and they depend on the medium properties at the scattering point. The details of the LAD technique are explained in Part II of this paper.

Using an asymptotic ray-based migration/inversion "point diffractor" operator, ray paths, slowness vectors, traveltimes, geometrical spreading and phase rotation factors are calculated from the image points up to the surface, forming a system for mapping the recorded surface seismic data into the LAD at the image points. The strength of the proposed imaging system is mainly in its ability to construct different types of high-quality angle-domain common-image gathers (ADCIG), representing continuous, full-azimuth, angle-dependent reflectivity in real 3D space.

First, we decompose the seismic recorded data into directional image gathers. Note that for each direction, seismic data events corresponding to ray pairs with the same orientation of the apparent reflection surface but different opening angles are accounted for in a weighted summation form. The directional gathers contain directivity-dependent information about specular and diffraction energy. Directional data decomposition is associated with what we call "diffraction imaging," which is under active research.

True amplitude imaging of point scatterers is extremely challenging. The asymptotic expansions for the amplitude behavior of point scatterers have been studied by de Vries et al. (1998) and recently by Wapenaar et al. (2010). Diffraction imaging in the prestack time domain has been intensively studied (e.g., Khaidukov et al., 2004; Bansal and Imhof, 2005; Shtivelman and Keydar, 2005; Fomel et al., 2006; Taner et al., 2006, and others). Kozlov et al. (2004) presented diffraction imaging in depth using a "side wave" Kirchhoff-type migration, where the migration aperture was tapered to filter out the specular energy. Moser and Howard (2008) presented the implementation of diffraction imaging in depth for 2D models, providing a comprehensive review and insight into the potential of diffraction waves to obtain high-resolution images of small-scale discontinuous subsurface objects. Recently, Reshef et al. (2009) showed that the shape of residual moveouts along diffractors within dip-angle gathers shows some similarities to specular reflectors along reflection-angle gathers. Thus, the diffraction energy within the dip-angle gathers can be used for high-resolution velocity analysis, especially in areas that contain discontinuous objects or along irregular interfaces. Note that in our study, dip-angle gathers are considered to be continuous, 3D, full-azimuth directional gathers.

The ability to decompose the specular and diffraction energy from the total scattered field obtained within the full-azimuth directional angle gathers is the core component of our proposed imaging system. It is based on estimating a directivity-dependent specularity attribute which measures the energy within calculated local Fresnel zones along the 3D directional gather. The directivity-dependent Fresnel zones are estimated using precomputed diffraction ray attributes, such as traveltimes, surface locations and slowness vectors. In practice, a specularity directional gather is computed for the corresponding seismic directional gather that also allows the extraction of structural subsurface attributes (e.g., dip, azimuth, and specularity/continuity) of the local reflecting/diffracting surfaces.

Note that this type of structural information normally is derived from postmigration images, created either by ray-based Kirchhoff or wave equation migrations, using local coherent event analysis or structure-oriented filters. In these migrations, the final image is constructed by stacking (averaging) a huge number of seismic events at each image point, accounting for the energy arriving at different opening angles and for all possible dips. This can result in smearing of the image along key subsurface objects, especially in complex geological areas characterized by faults, pinchouts and material discontinuities. Thus, it is clear that the standard coherence methods used for extracting the above-mentioned structural information suffer from inaccuracy, instability, and considerable uncertainty.

The energy (or specularity measurement) computed along the directional angle gather values also is used as a weighted stack operator. Two types of images are constructed: specular weighted stacks for emphasizing subsurface structure continuity, and diffraction weighted stacks, which emphasize discontinuities of small-scale objects such as faults, channels and fracture systems. Note that full-azimuth directional angle decomposition does not necessarily require a wide-azimuth acquisition geometry system; rather, a large migration aperture is needed to allow information from all directions. Moreover, in many cases it is sufficient to use small offsets to create directional angle gathers. For example, it has been shown that nearly vertical faults and salt flanks can be detected via simulated corner (duplex) waves established with directional angle decomposition, where the integration is performed on narrow opening angles (narrow cones) only (Kozlov et al., 2009).

Once background directivity is derived, full-azimuth reflection-angle gathers are created by integrating all the dip/azimuth angles around that direction. Note that if the certainty about the background directivity is high (measured by the specularity criteria), only a small dip-angle range around the background direction (estimated from the angle-dependent Fresnel zone) is required to capture the specular energy. The specularity criterion is a measure of the energy concentration along the directional angle gathers. The seismic data reflected/diffracted from the image points are decomposed/binned into common opening (reflection/diffraction) angles and opening azimuth angles. The full-azimuth reflection-angle gathers are used to extract residual moveouts (RMO), which measure the accuracy of the background velocity model used. The full-azimuth RMO, together with the directivity information, comprises the required set of input data for velocity model determination via tomographic solutions. In addition, the true amplitude, full-azimuth, reflection-angle gathers serve as optimal data for amplitude analysis (AVAZ), and for the extraction of high-resolution elastic properties. For these kinematic and dynamic types of analysis, long offsets and rich azimuths are particularly effective.

FULL-AZIMUTH SUBSURFACE ANGLE-DOMAIN DECOMPOSITION: DIRECTIONAL AND REFLECTION GATHERS

Our approach consists of three main stages: Ray tracing, full-azimuth angle-domain decomposition, and final imaging (weighted stacks). The ray tracing stage involves shooting a fan of one-way diffraction rays from image points up to the surface.

The take-off angles are measured around a given local normal to a background reflection surface (if the background directivity is unavailable, the vertical axis is assumed). Ray attributes, such as traveltime, ray coordinates, slowness vectors, amplitude and phase factors, are stored for each ray. The full-azimuth angle-domain decomposition stage involves forming a combination of ray pairs indicating incident and reflected/diffracted rays. Each ray pair maps a specific seismic data event, recorded on the acquisition surface, into a 4D local angle-domain space in the subsurface — dip and azimuth of the ray pair normal, opening angle and opening azimuth (see Figure 2). The term "ray pair normal" refers to an apparent normal (also called migration dip vector) computed from Snell's law for any isotropic or anisotropic velocity model, where both incident and scattered slowness directions are known. This is a normal to a virtual surface formed by the incident and scattered rays. Note that the specular direction indicates the special case when the ray pair normal coin-

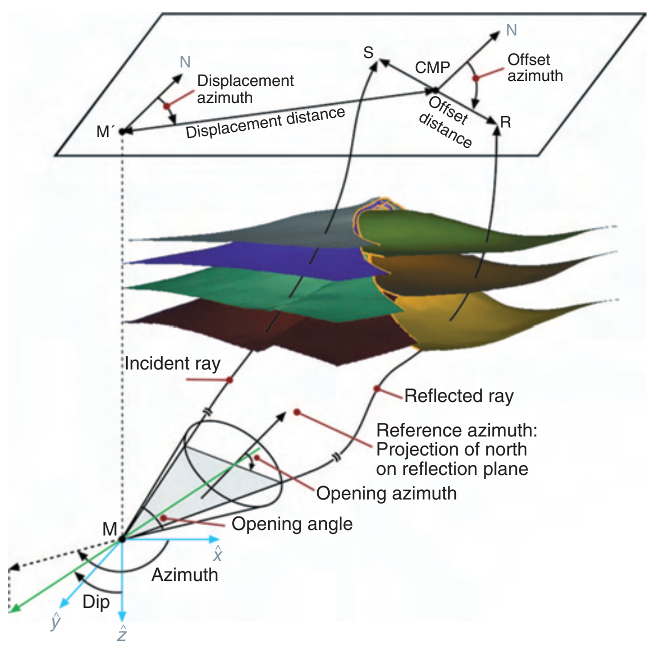

Figure 2. Subsurface-to-surface and surface-to-subsurface ray-based mapping. Each ray pair maps a specific seismic data event recorded on the acquisition surface, into a 4D local angle-domain space in the subsurface — dip and azimuth of the ray pair normal, opening angle and opening azimuth.

cides with the normal to a physical reflection surface (see details in Part II of this paper).

The four source-receiver surface coordinates (two for the source, two for the receiver) are defined according to their displacement vector and offset vector. Each vector is defined by its magnitude and azimuth, where the displacement magnitude is the horizontal distance between the source-receiver midpoint and the image location (also referred to as migration aperture distance). Note that theoretically each of the four surface parameters depends on all four LAD angles, and vice versa. There is, however (especially in moderately complex models) a stronger dependency between the directional angle gathers and the displacement vector, and between the opening angles and the offset vector.

The mapping of the surface data U into the subsurface angle domain

$$U(\mathbf{S},\mathbf{R},t)\rightarrow I(\mathbf{M},\nu_1,\nu_2,\gamma_1,\gamma_2), \tag{1}$$

where $\mathbf{M}$ is the subsurface image point, and $\mathbf{S}=\{S_x,S_y\}$, $\mathbf{R}=\{R_x,R_y\}$ are the source and receiver locations, involves generating 7D angle-domain data (four angles per subsurface point). This process requires a massive amount of memory throughout the mapping process and a huge amount of disk space to store the results.

Although this type of mapping (decomposition) can be extremely valuable for enhancing the imaging and analysis of seismic data, it still is considered unfeasible even with the largest available computers. We therefore propose splitting the general decomposition process into two complementary angle-domain image gathers, directional and reflection. At each subsurface point, these image gathers become functions of only two angles, where integration over the other two angles is performed. We follow the derivation of GRT imaging, described in the introduction to this paper.

Directional and reflection seismic gathers

In the directional seismic gathers, the reflectivity/diffractivity I_ν at the image point is a function of the ray pair normal dip ν_1 and azimuth ν_2,

$$I_\nu(\mathbf{M},\nu_1,\nu_2)=\int K_\nu(\mathbf{M},\nu_1,\nu_2,\gamma_1,\gamma_2)H^2\sin\gamma_1 d\gamma_1 d\gamma_2, \tag{2}$$

where K_ν is the kernel of the directional integrand,

$$K_\nu(\mathbf{M},\nu_1,\nu_2,\gamma_1,\gamma_2)=W_\nu(\mathbf{M},\nu_1,\nu_2,\gamma_1,\gamma_2)\cdot L(\mathbf{M},\nu_1,\nu_2,\gamma_1,\gamma_2), \tag{3}$$

W_ν is the integration weight for directional angle gather, explained below, and L is the filtered and amplitude-weighted input data,

$$L(\mathbf{M},\nu_1,\nu_2,\gamma_1,\gamma_2)=\frac{D_3(\mathbf{S},\mathbf{R},\tau_D)}{A(\mathbf{M},\mathbf{S})A(\mathbf{M},\mathbf{R})}, \tag{4}$$

and H is the obliquity factor, depending primarily on the opening angle γ_1 and explained below. The term "diffractivity" is used here to indicate the reflectivity at nonspecular directions. In the reflection-angle gathers, the reflectivity I_γ at the image point is a function of the opening angle γ_1 and the opening azimuth γ_2,

$$I_\gamma(\mathbf{M},\gamma_1,\gamma_2)=\int K_\gamma(\mathbf{M},\nu_1,\nu_2,\gamma_1,\gamma_2)H^2\sin\nu_1 d\nu_1 d\nu_2, \tag{5}$$

where K_γ is the kernel of the reflection integrand,

$$K_\gamma(\mathbf{M},\nu_1,\nu_2,\gamma_1,\gamma_2)=W_\gamma(\mathbf{M},\nu_1,\nu_2,\gamma_1,\gamma_2)\cdot L(\mathbf{M},\nu_1,\nu_2,\gamma_1,\gamma_2), \tag{6}$$

and W_γ is the integration weight for reflection-angle gather, explained below. Thus in both directional and reflection-angle gathers, the integrands include the kernels, the obliquity factor and area elements on the spherical surface. For directional angle gathers, the integration limits are from zero to maximum opening angle $\gamma_1^{\max}$, and for reflection-angle gathers, the integration limits are from zero to maximum dip angle of the ray pair normal $\nu_1^{\max}$, where both upper limits are, of course, less than π. In the azimuthal dimension, the integration includes full azimuths, i.e., from zero to 2π for both γ_2 and ν_2. The obliquity factor H in equation 2 and equation 5 is the magnitude of the slowness sum of the incident and reflected rays, i.e., the absolute value of the two-way traveltime gradient, which decays with increasing opening angle γ_1,

$$H=\frac{\sqrt{V_S^2(\mathbf{M})+V_R^2(\mathbf{M})+2V_S(\mathbf{M})V_R(\mathbf{M})\cos\gamma_1}}{V_S(\mathbf{M})V_R(\mathbf{M})}=|\nabla\tau_D|. \tag{7}$$

The expressions $V_S(\mathbf{M})$ and $V_R(\mathbf{M})$ are the phase velocities of the incident and scattered rays, respectively, at the image point. In particular, for an isotropic case, the velocities of the two rays are equal, and the obliquity factor reduces to

$$H=\frac{2}{V(\mathbf{M})}\cos\frac{\gamma_1}{2}. \tag{8}$$

When the opening angle between the two rays approaches straight angle $\gamma_1^{\max}\rightarrow\pi$, the obliquity factor vanishes. Indeed, it follows from equation 7,

$$\lim_{\gamma_1\rightarrow\pi} H=\left|V_S^{-1}(\mathbf{M})-V_R^{-1}(\mathbf{M})\right|. \tag{9}$$

Furthermore, straight opening angle means propagation of the incident and reflected rays along the same line, and in this case their phase velocities are equal for a general anisotropy, $V_S(\mathbf{M})=V_R(\mathbf{M})$.

In our notation, both rays are assumed arriving from the surface to the subsurface image point. Locations

$$\mathbf{S}=\mathbf{S}(\mathbf{M},\nu_1,\nu_2,\gamma_1,\gamma_2),\quad \mathbf{R}=\mathbf{R}(\mathbf{M},\nu_1,\nu_2,\gamma_1,\gamma_2) \tag{10}$$

are the source and receiver coordinates on the acquisition surface(s). These coordinates are established by the traced one-way diffraction rays that connect the given image points with the given source and receiver locations. The dependency of the source and receiver locations on the background velocity model and the set of LAD angles for each image point makes the implementation of this output-driven approach extremely difficult. Parameters

$$A(\mathbf{M},\mathbf{S}) = \frac{1}{4\pi}\cdot\sqrt{\frac{\sin\beta_1^S(\mathbf{M})}{V_S(\mathbf{M})|J(\mathbf{M},\mathbf{S})|}},$$

$$A(\mathbf{M},\mathbf{R}) = \frac{1}{4\pi}\cdot\sqrt{\frac{\sin\beta_1^R(\mathbf{M})}{V_R(\mathbf{M})|J(\mathbf{M},\mathbf{R})|}} \tag{11}$$

are the amplitudes of Green's functions (e.g., Bleistein et al., 2001), where J is the ray Jacobian,

$$J = \frac{d\mathbf{x}}{d\sigma}\cdot\frac{d\mathbf{x}}{d\beta_1}\times\frac{d\mathbf{x}}{d\beta_2}. \tag{12}$$

Parameter σ is an integration characteristic along the ray, with units $[\sigma]=\mathrm{m}^2\cdot\mathrm{s}^{-1}$ (m for meter and s for second), so that $[J]=\mathrm{m}\cdot\mathrm{s}$, and $[A]=\mathrm{m}^{-1}$. Angles β_1 and β_2 are dip and azimuth of the take-off direction at the image point.

The filtered version of the data is (Bleistein et al., 2001; Bleistein and Gray, 2002; Koren et al. 2002),

$$D_3[\mathbf{S},\mathbf{R},\tau_D(\mathbf{S},\mathbf{M},\mathbf{R})] = \frac{1}{2\pi B}\int_{-\infty}^{+\infty} iwU(\mathbf{S},\mathbf{R},w)\exp(i\Phi_3)dw, \tag{13}$$

where w is the temporal frequency. Parameter Φ_3 is the phase,

$$\Phi_3 = w\tau_D(\mathbf{S},\mathbf{M},\mathbf{R}) - \frac{\pi}{2}K(\mathbf{S},\mathbf{M},\mathbf{R})\mathrm{sgn}(w), \tag{14}$$

and $U(\mathbf{S},\mathbf{R},w)$ is the input seismic trace in the frequency domain,

$$U(\mathbf{S},\mathbf{R},w) = \int_0^{\infty} U(\mathbf{S},\mathbf{R},t)\exp(-iwt)dt. \tag{15}$$

Assuming arbitrary units $[U]$ for the recorded wavefield in the time domain, the wavefield units in the frequency domain are $[U]\cdot\mathrm{s}$. Factor B in equation 13 is the amplitude of the point-source power, representing the constant ratio between the incident field in the frequency domain and the corresponding Green's function; its units are $[B]=[U]\cdot\mathrm{m}\cdot\mathrm{s}$. Thus, the units of the filtered data are $[D_3]=\mathrm{m}^{-1}\cdot\mathrm{s}^{-2}$. The units of amplitude-weighted data in equation 4 become $[L]=\mathrm{m}\cdot\mathrm{s}^{-2}$, and the same are the units of the kernels K_ν and K_γ. Finally the units of the estimated "reflectivity" in equation 2 and equation 5 are $[I]=\mathrm{m}^{-1}$. The estimated "reflectivity" can be interpreted as $I=R\delta(s-s_o)$, where R is the actual (unitless) reflectivity, and $\delta(s-s_o)$ is 1D Dirac delta-function of normal signed distance $s-s_o$ from the reflector located at s_o (Bleistein and Gray, 2002).

Parameter $K(\mathbf{S},\mathbf{M},\mathbf{R})$ is the KMAH index, and $\tau_D=\tau_D(\mathbf{S},\mathbf{M},\mathbf{R})$ is the diffraction stack time. The KMAH index counts the number of caustics along the traced rays. Recall that caustics refer to points along the ray where the determinant of the Jacobian matrix vanishes. Two cases of caustic are distinguished: Jacobian matrix of rank two (instead of three at regular points), where the area of the ray tube section collapses to a line (incrementing KMAH by one), and rank one, where the area collapses to a point (incrementing KMAH by two).

Equation 15 is the forward real-to-complex Fourier transform of the input trace U from the time domain to the frequency domain. Multiplying the transformed signal by iw, we get the transformed derivative. Thus, in the absence of caustics, the inverse transform on the right side of equation 13 converts the derivative of the input from the frequency domain to the time domain. Caustics modify the phase for the inverse complex-to-real transform according to equation 14. The absolute KMAH index is not essential, but its remainder on division by four is. Remainders zero and two yield the derivative of data, with the original and opposite sign, respectively. Remainders one and three yield the Hilbert transform of the derivative, also with the original and opposite sign, due to the relationship between the Fourier transform F and the Hilbert transform HT,

$$F[HT(P)] = -i\,\mathrm{sgn}(w)\cdot F[P] \quad \text{or}$$

$$HT(P) = F^{-1}[-i\,\mathrm{sgn}(w)\cdot F(P)], \tag{16}$$

where P is an arbitrary function; in our case $P=\partial U/\partial t$. Recall that after the Hilbert transform, the function remains in the same (time) domain.

Functions $W_\nu(\mathbf{M},\nu_1,\nu_2,\gamma_1,\gamma_2)$ and $W_\gamma(\mathbf{M},\nu_1,\nu_2,\gamma_1,\gamma_2)$ are integration weights, inversely proportional to the hit counts (illumination). Weight $W_\nu(\mathbf{M},\nu_1,\nu_2,\gamma_1,\gamma_2)$ is estimated for any fixed directional dual angle ν_1,ν_2 and for a defined proximity of the running reflection dual angle γ_1,γ_2 as shown in Figure 3a. Similarly, the integration weight $W_\gamma(\mathbf{M},\nu_1,\nu_2,\gamma_1,\gamma_2)$ is estimated for any fixed reflection dual angle γ_1,γ_2 and for a defined proximity of the running directional dual angle ν_1,ν_2 as shown in Figure 3b. The proximity is a circle of a preselected radius on the unit sphere (solid angle), where the center of the circle corresponds to the running value.

The scheme for computing the integration weights is presented in Figure 4. When the integration through the reflection sphere is performed, the running dual angle γ_1,γ_2 (black dashed line) is the center of the circular proximity of radius β_γ, and $\tilde{\gamma}_1,\tilde{\gamma}_2$ (red solid lines) are the dual reflection angles of multiple ray pairs inside this region. Similarly, on the directional sphere, the running angle ν_1,ν_2 is the center of the proximity of radius β_ν, and $\tilde{\nu}_1,\tilde{\nu}_2$ are multiple dual direction angles inside,

$$\sin^2\frac{\tilde{\gamma}_1-\gamma_1}{2} + \sin\tilde{\gamma}_1\sin\gamma_1\sin^2\frac{\tilde{\gamma}_2-\gamma_2}{2} \le \sin^2\frac{\beta_\gamma}{2} = \frac{A_\gamma^{\mathrm{solid}}}{4\pi}$$
$$\sin^2\frac{\tilde{\nu}_1-\nu_1}{2} + \sin\tilde{\nu}_1\sin\nu_1\sin^2\frac{\tilde{\nu}_2-\nu_2}{2} \le \sin^2\frac{\beta_\nu}{2} = \frac{A_\nu^{\mathrm{solid}}}{4\pi}, \tag{17}$$

where the right sides are ratios of the proximity areas (solid angles) to the area of the entire sphere 4π.

The rays are shot from the image point and distributed evenly in all directions, so that the given area of the proximity is equivalent to the fixed number of rays whose starting angles are within the proximity radius. Because of the limited migration aperture, acquisition geometry, and complexity of the background velocity model for each value of a running dual angle, some of the rays in the proximity reach the earth's surface within the given recording aperture, whereas others do not.

The weight is the ratio of the total number of rays in proximity to the number of arrivals (assuming there is at least one arrival). The ratio of the total number of rays to the number of arrivals is related to the ratio of the total wavefield amplitude (from the LAD proximity) to the amplitude of the rays (from the same proximity) that reach the recording aperture. The greater the number of arrivals, the smaller the weight. Note that the illumination weights are 4D arrays per each image point, or 5D arrays for each gather with a fixed inline-crossline location. The illumination weights need to be computed prior to the migration stage, and stored in memory for implementation throughout the integration.

As noted above, equation 2 and equation 5 present an output-driven approach, where the input seismic data used for the migration become functions of the LAD angles at the image points (equation 10). The problem in this type of approach is that every ray pair used in the migration requires random access to a different seismic trace within the massive amount of input data, making the I/O process very costly and difficult to implement. In addition, this approach requires a huge amount of memory for storing the input data and the computational arrays. In our implementation, we overcome this obstacle by dividing the subsurface into small subvolumes, each independently migrated using a parallel computation process. This process, together with a special discretization of the 4D LAD space, dramatically reduces the size of the computational arrays and output data.

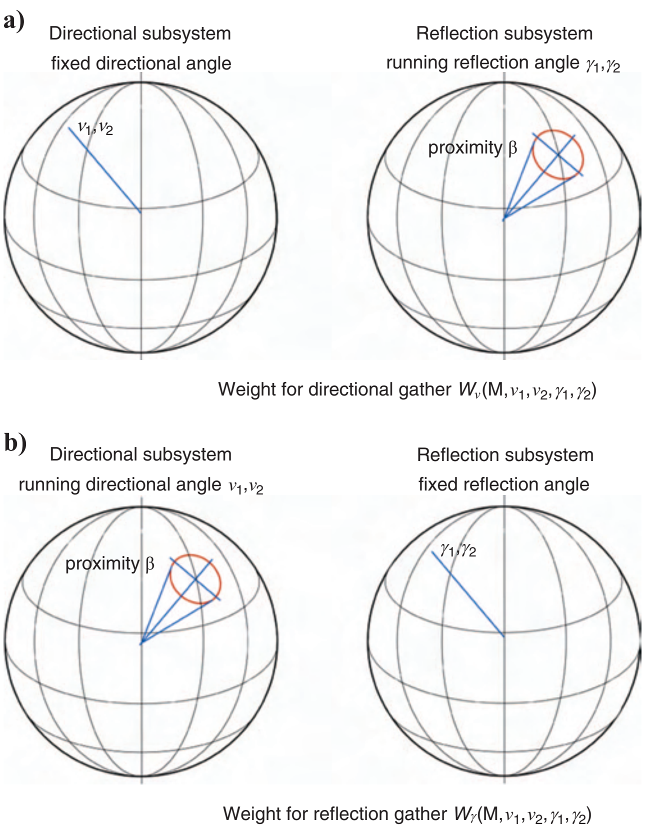

Figure 3. Scheme for integration weights inversely proportional to hit counts; β is the cone angle of the proximity on the spherical surface. (a) Weight for directional angle gather, $W_\gamma(\mathbf{M},\nu_1,\nu_2,\gamma_1,\gamma_2)$. Dual directional angle ν_1,ν_2 is fixed, whereas dual reflection angle γ_1,γ_2 is running. Hit counts are calculated for rays whose starting directions in the subsurface are in β-proximity of the running reflection angle. (b) Weight for reflection-angle gather, $W_\nu(\mathbf{M},\nu_1,\nu_2,\gamma_1,\gamma_2)$. Dual reflection angle γ_1,γ_2 is fixed, whereas dual directional angle ν_1,ν_2 is running. Hit counts are calculated for rays whose starting directions in the subsurface are in β-proximity of the running directional angle.

Local slant stacks and beam steering

Gaussian beam migrations (e.g., Hill, 2001; Gray and Bleistein, 2009; Gray et al., 2009) have been implemented successfully in improving Kirchhoff-based migrations in complex geological areas, especially where the wavefield includes multipathing. Fast beam-steering migrations (e.g., Sherwood et al., 2009) have become very popular also, especially for velocity model building where only the energetic beams are stored and used. These beam migrations require preprocessing of the recorded seismic data traces prior to the migration.

The construction of beams is based on a local tapered slant stack approach, which normally is performed for a coarse grid, depending on the dominant frequency of the input data. The local slant stack approach normally enhances signal-to-noise ratio, and therefore improves continuity of the structural image. Note that every beam event is associated with traveltime, shot-receiver areas and directivity. In our implementation, the creation and migration of beams also are enabled. However, the beams are performed on the fly throughout the decomposition/imaging stage, where for each ray pair, a set of proximity sources around the "source ray" and the corresponding receivers at the vicinity of the "receiver ray" are collected to form the slant stack process.

The Gaussian beam is presented schematically in Figure 5, where for simplicity only a single source is shown. In practice, however, we deal with a bunch of sources in the vicinity of each "source ray" The proximity for each ray is computed individually with the estimated local Fresnel zone. The Fresnel zones are assumed to be elliptic projections of circular regions around the central source ray and the central receiver ray on the earth's surface, with major semiaxes $R_F^{\text{maj}}(\mathbf{M,S})$ and $R_F^{\text{maj}}(\mathbf{M,R})$, respectively,

$$R_F^{\text{maj}}(\mathbf{M,S}) = \sqrt{\frac{\sigma'(\mathbf{M,S})}{f_D}}, \quad R_F^{\text{maj}}(\mathbf{M,R}) = \sqrt{\frac{\sigma'(\mathbf{M,R})}{f_D}}, \tag{18}$$

where parameter σ' approximates the geometrical spreading,

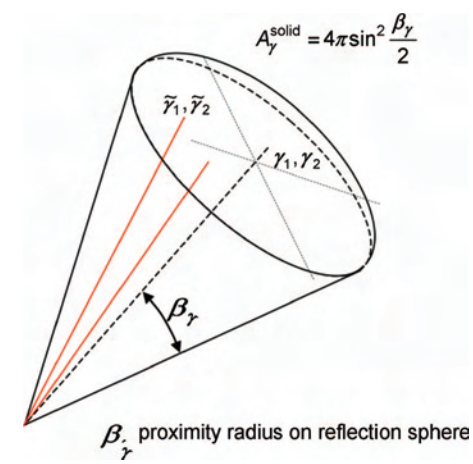

Figure 4. The solid angle defines the circular proximity on the surface of a reflection sphere. Central direction of proximity is shown by black dashed line. Rays with starting angles inside the proximity are shown by red solid lines.

$$\sigma'(\mathbf{M},\mathbf{S}) = \sqrt{|J(\mathbf{M},\mathbf{S})|V^3(\mathbf{S})},$$

$$\sigma'(\mathbf{M},\mathbf{R}) = \sqrt{|J(\mathbf{M},\mathbf{R})|V^3(\mathbf{R})}, \qquad (19)$$

with the units $[\sigma'] = \mathrm{m}^2/\mathrm{s}$. For each ray ("source" and "receiver"), the ratio between the minor and major semiaxes depends on the dip angle ν_1^{surf} of the phase velocity at the earth surface point, $R_F^{\min}/R_F^{\mathrm{maj}} = \cos\nu_1^{\mathrm{surf}}$, and the eccentricity of the elliptic zone is $\xi_F = \sin\nu_1^{\mathrm{surf}}$. In case of a tilted topographic surface, we replace the dip angle ν_1^{surf} with the angle between the phase velocity and the normal to the topography. Thus the area of the proximity $A_F = \pi R_F^{\min}R_F^{\mathrm{maj}}$ is estimated from the ray Jacobian J of each individual ray and the dominant frequency f_D of the recorded data. The slant (slope) used for the local stack is taken from the slowness vectors of the "source ray" $\mathbf{p}^S$ and the "receiver ray" $\mathbf{p}^R$, respectively. The local tapered slant stack event can be constructed by

$$U_{\mathrm{beam}}(\mathbf{S}_o,\mathbf{R}_o,t) = \frac{1}{N_f}\int\int_{\partial S\partial R} U(\mathbf{S}_o + \Delta\mathbf{S},\mathbf{R}_o + \Delta\mathbf{R},t + \Delta\tau) f_{\mathrm{taper}}(\Delta\mathbf{S},\Delta\mathbf{R})d\mathbf{S}d\mathbf{R}, \qquad (20)$$

where N_f is a normalization factor, $\Delta\mathbf{S} = \{\Delta x_S,\Delta y_S,\Delta z_S\}$, $\Delta\mathbf{R} = \{\Delta x_R,\Delta y_R,\Delta z_R\}$ are the shifts between central and "current" locations of sources/receivers of the stacked traces within the local areas bounded by the Fresnel zones, along the acquisition surface $z = z(x,y)$. Function $U(\mathbf{S}_o + \Delta\mathbf{S},\mathbf{R}_o + \Delta\mathbf{R},t + \Delta\tau)$ is the recorded seismic data, $t = t(\mathbf{M},\mathbf{S}_o,\mathbf{R}_o)$ is the two-way traveltime of the central rays, $f_{\mathrm{taper}}(\Delta\mathbf{S},\Delta\mathbf{R})$ is a Gaussian taper, and $\Delta\tau$ is the traveltime correction due to the above-mentioned shifts,

$$\Delta\tau = \Delta\tau_S + \Delta\tau_R = p_x^S\Delta x_S + p_y^S\Delta y_S + p_z^S\Delta z_S + p_x^R\Delta x_R + p_y^R\Delta y_R + p_z^R\Delta z_R. \qquad (21)$$

Thus, the construction of the local beams to be migrated for each point and each ray pair theoretically is more accurate than the standard beam migrations, where the beam construction is performed uniformly prior to the migration. A beam steering approach can then be applied by measuring the coherency (e.g., semblance) of the candidate wavelets before the performance of the slant stack, where only energetic events are migrated.

Specularity directional gathers

One of the main goals of this work is to provide a method for separating the specular energy from the total scattered field along the seismic directional gathers. It is assumed that in the actual specular direction, ν_1^*,ν_2^*, the coherency measure (semblance) along reflection events, from all available opening angles γ_1 and opening azimuths γ_2, is larger than that along nonspecular directions. To estimate the semblance for each direction, two auxiliary directional angle gathers are computed: energy and hit count. The energy directional angle gather is computed by integrating the direction kernel squared through all reflection angles,

$$E_\nu(\mathbf{M},\nu_1,\nu_2) = \int K_\nu^2(\mathbf{M},\nu_1,\nu_2,\gamma_1,\gamma_2)H^4 \times\sin\gamma_1 d\gamma_1 d\gamma_2, \qquad (22)$$

where the kernel K_ν and the obliquity factor H are defined in equation 3 and equation 7, respectively. Note that all of the three directional angle gathers — seismic $I_\nu(\mathbf{M},\nu_1,\nu_2)$, energy $E_\nu(\mathbf{M},\nu_1,\nu_2)$, and hit count $N_\nu(\mathbf{M},\nu_1,\nu_2)$, — are computed in the same imaging process. The specularity (semblance) gather then is computed from these gathers as follows,

$$f_{\mathrm{spec}}(\mathbf{M},\nu_1,\nu_2) = \frac{1}{N(\mathbf{M},\nu_1,\nu_2)}\cdot\frac{I_\nu^2(\mathbf{M},\nu_1,\nu_2)}{E_\nu(\mathbf{M},\nu_1,\nu_2)}. \qquad (23)$$

In the following section, we show field examples of computed specularity directional gathers and their application: extracting high-resolution structural dip and azimuth information, and generating different types of images using specular/diffraction weighted stacks.

Full-azimuth angle-domain common-image gathers

Figure 6 displays a schematic example of the full-azimuth angle-domain common-image gathers. Figure 6a shows a depth migrated section from 3D land data. The vertical line shows a lateral (inline-crossline) location of a specific gather, with an image point in depth marked on this line. A reflection-angle gather at this location, in a given azimuth, is shown in Figure 6b. Figure 6c shows two spherical displays related to the specific image point. The sphere on the right represents the specular and diffused energy as a function of the dip/azimuth direction. The location of the spot on the sphere indicates that the image point is located in the vicinity of an actual reflecting surface. The orientation of the local reflecting surface is defined by the dip/azimuth indicated by the maximum energy value.

For a real reflector, the size of the spot on the directional image normally is a relatively small area in the proximity of the specular direction. The specular component is attenuated relative to the scattered component. Thus, the size of the spot relates to the measure of the energy concentration, where in the vicinity of a real reflector,

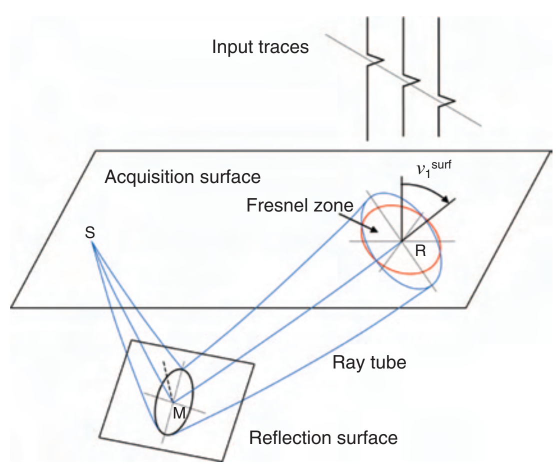

Figure 5. Gaussian beam migration scheme with a single source. The blue circle (viewed as an ellipse) is the normal cross section of the beam at the arrival point of the central ray. The red ellipse is the projection of the blue circle on the acquisition surface, and it represents the Fresnel zone. The major semiaxis of the red ellipse is equal to the radius of the blue circle. The minor semiaxis depends on the dip angle of the central ray at the arrival point, ν_1^{surf}.

most of the energy will be concentrated in the specular direction, and in the vicinity of diffractors, low energy will be distributed in all directions.

The sphere on the left represents the reflectivity versus the opening angle and opening azimuth. For a real reflector, high amplitudes are displayed along a relatively large opening angle range that depends on the illumination quality caused by the complexity of the velocity model and the data acquisition. The north pole on the directional sphere represents the dip direction coinciding with the background reference dip, whereas the north pole on the reflection sphere represents zero offset or zero opening angle. Figure 6d is a cylindrical display related to all vertical points of the gather. These points have a fixed lateral location and different depths. The cylindrical display includes a stack of disks, where each disk is related to a specific point in depth. The disk image is obtained from the spherical image by projecting or expanding the spherical surface on a plane.

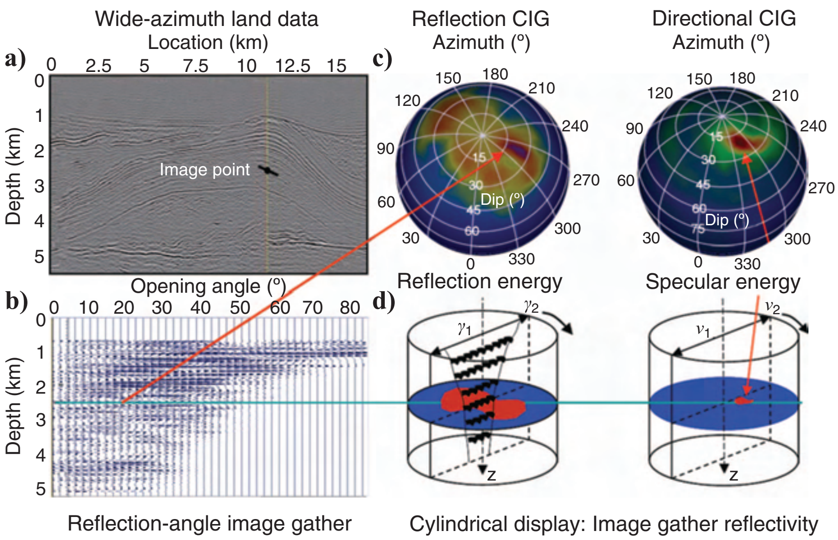

Figure 6. Schematic example of full-azimuth angle-domain common-image gathers: directional and reflection. (a) Depth migrated section from 3D land data, with a lateral location of a specific gather shown by the vertical line and an image point in depth marked on this line. (b) Reflection-angle gather at this lateral location, in a given azimuth. (c) Reflection and directional spherical displays related to a specific image point. The north pole on the directional sphere represents the dip direction coinciding with the background reference dip, and the north pole on the reflection sphere represents zero offset or zero opening angle. (d) Cylindrical display related to all vertical points of the gather.

Recommended workflow

Our implementation enables the simultaneous generation of the two full-azimuth angle gathers: directional and reflection. In practice, however, we recommend a very specific workflow.

First, generate directional angle gathers with relatively small opening angles (integrating only data points with moderate ray pair opening angles, for example, below ~60°). The directional angle gathers require the availability of data from rich directions (large migration aperture), but not necessarily wide-opening angles or wide-opening azimuths. Specularity directional angle gathers then can be constructed, and specular directions (dip and azimuth) of actual local reflecting surfaces can be extracted.

Second, generate reflection-angle gathers in the specular direction, using a small dip range (migration aperture), with wide opening angles and all opening azimuths to maximize the available information on the angle-dependent reflectivity. Full-azimuth subsurface angle-domain residual moveouts (RMO) then can be automatically picked for high-resolution anisotropic tomographic velocity updating. In addition, amplitude versus angle and azimuth analysis (AVAZ) can be performed to enhance reservoir imaging and characterization, in particular, fracture detection.

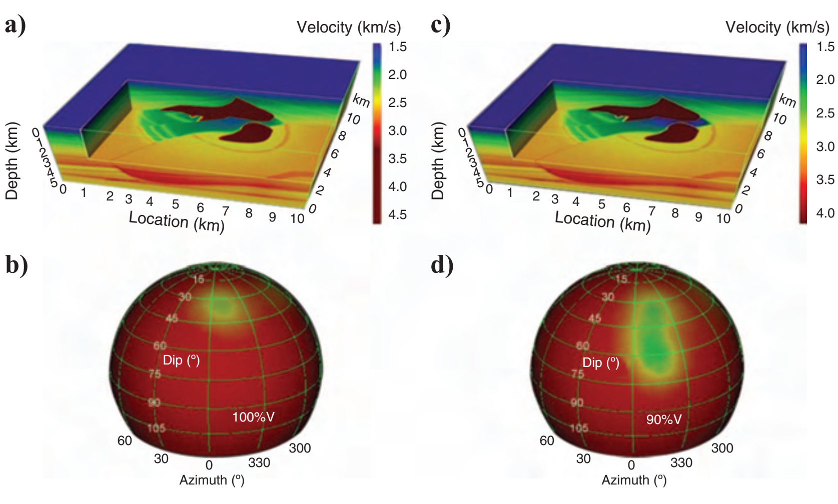

Figure 7. Velocity model accuracy. (a) True velocity model of the SEG/EAGE salt model. (b) Specularity as a function of dip/azimuth angles at a reflecting surface below salt. (c) Same velocity model with a 10% velocity error applied in region below salt. (d) Corresponding directional specularity.

VELOCITY MODEL ACCURACY USING DIRECTIONAL GATHERS

Figure 7a shows the actual true velocity model of the SEG/EAGE salt model. Using directional angle decomposition, the specularity as a function of the dip/azimuth angles at a given reflecting surface below the salt is shown in Figure 7b. The specularity is displayed as a small spot concentrated in the vicinity of the actual directivity of the given reflector.

Figure 7c shows the same velocity model when a 10% velocity error was applied in the region below the salt. The corresponding directional specularity is shown in Figure 7d. It is clear that the energy is smeared (defocused) along the directional unit sphere, indicating the error in the velocity model and hence the directivity of the given reflector.

This example suggests a procedure for quickly evaluating the integrity of the velocity model. Note that this directivity focusing-analysis approach is considered a complementary approach to the universally used velocity model error analysis, based on measuring residual moveouts along reflection-angle gathers.

FIELD EXAMPLES

In this section, we provide field examples of directional-based and reflection-based decomposition for enhancing velocity model determination, and for extracting high-resolution structural attributes.

Example A

Example A shows directional-based imaging using 3D land data from Egypt, where the subsurface model is characterized by dominant overthrust. Figure 8 shows an example of a cylindrical specularity directional angle gather, where the specular energy (directivity-dependent Fresnel volume) is emphasized. The high amplitudes of the specular energy along the vertical axis indicate the directivity changes of the subsurface reflectors with depth.

Figures 9a and 10a show the imaging results of the inline and crossline sections, respectively, using traditional Kirchhoff-based migrations. Figures 9b and 10b show the markedly improved results obtained when using the specular energy shown in Figure 8 as the directional weighted stack operator,

$$I_{\text{spec}}(\mathbf{M}) = \sum_{\nu_1,\nu_2} I_\nu(\mathbf{M},\nu_1,\nu_2)\cdot f^p_{\text{spec}}(\mathbf{M},\nu_1,\nu_2), \qquad (24)$$

where $f_{\text{spec}}(\mathbf{M},\nu_1,\nu_2)$ is the specularity gather that measures the high-energy reflectivity from continuous surfaces, defined by equation 23, and p is an amplifying power index. Each data point in the specularity gather is a measure of the energy concentration computed along the directional angle gather, with a given 3D window — dip, azimuth and depth (Koren et al., 2010). Figure 11a shows the specular weighted energy stack at a given line, and views 11b-d show the same image with an overlay of the extracted structural attributes — dip, azimuth and continuity. Figure 12 shows these attributes for the entire volume at a given depth.

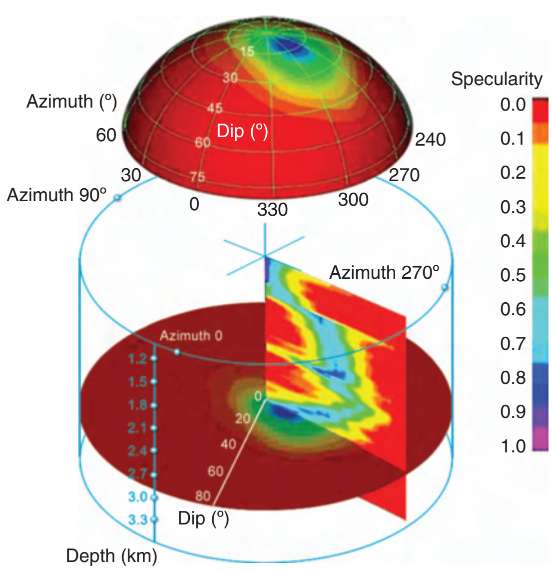

Figure 8. 3D cylindrical specularity directional angle gather.

Example B

Figure 13 shows two depth migrated sections from 3D land data in northwest Germany (owned by RWE-Dea AG and Wintershall AG) following the creation of directional angle gathers. Figure 13a shows the direct stack of the directional angle gathers, and Figure 13b the specular energy weighted stack of the same gathers. The high energy values associated with the specular directions sharpen the image of

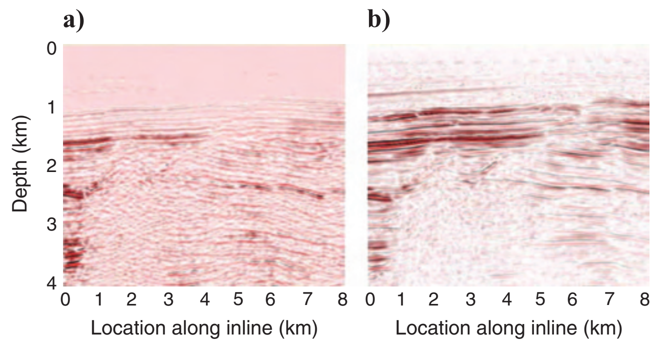

Figure 9. Comparison between two images of the same inline. (a) Kirchhoff migration. (b) Specular weighted energy stack along directional angle gathers.

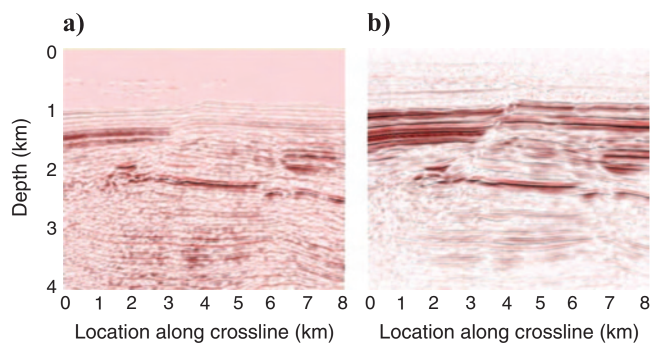

Figure 10. Comparison between two images of the same crossline. (a) Kirchhoff migration. (b) Specular weighted energy stack along directional angle gathers.

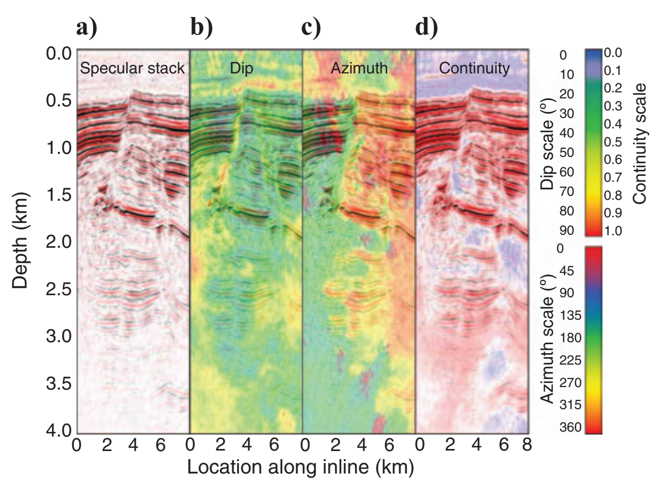

Figure 11. Depth section along a given line. (a) Specular weighted energy stack. (b) Specular weighted energy stack with dip overlay. (c) Specular weighted energy stack with azimuth overlay. (d) Specular weighted energy stack with continuity overlay.

the structure, and the improvement in the continuity of the structural information throughout the volume is seen clearly in Figure 13b.

Figure 14 shows an example of a specularity directional angle gather in the vicinity of the salt. Two areas of specular energy are clearly visible, indicating subsurface points which are in the vicinity of conflicting dips, such as unconformities and pinchouts. This shows that the common assumption that every image point is characterized by single directivity is somewhat naïve, and that we also must consider all the energetic directions.

Example C

Figure 15 shows an example of imaging in a complex basin in offshore Australia. Using directional angle decomposition and specular energy weighting, we were able to detect and image a structure (Figure 15b) that previously was completely hidden due to noisy data in nonspecular directions (Figure 15a).

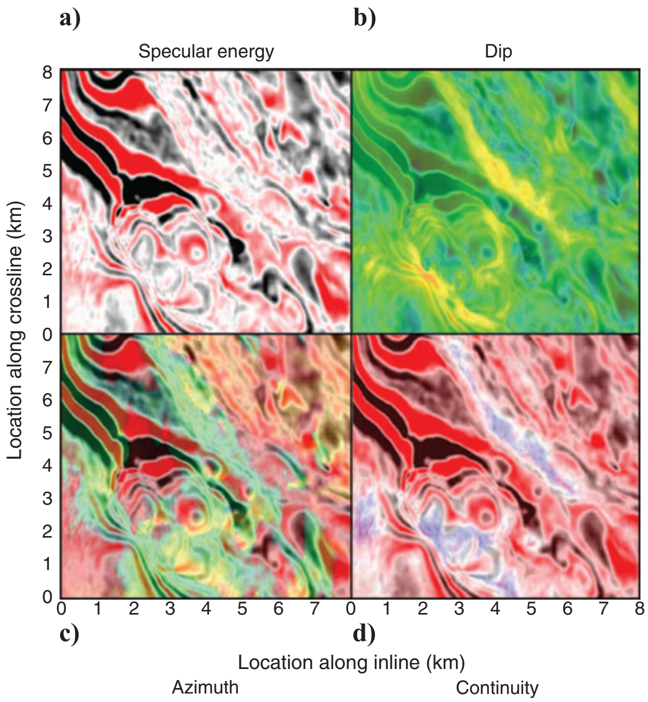

Figure 12. Depth slice throughout 3D image. (a) Specular weighted energy stack. (b) Specular weighted energy stack with dip overlay. (c) Specular weighted energy stack with azimuth overlay. (d) Specular weighted energy stack with continuity overlay.

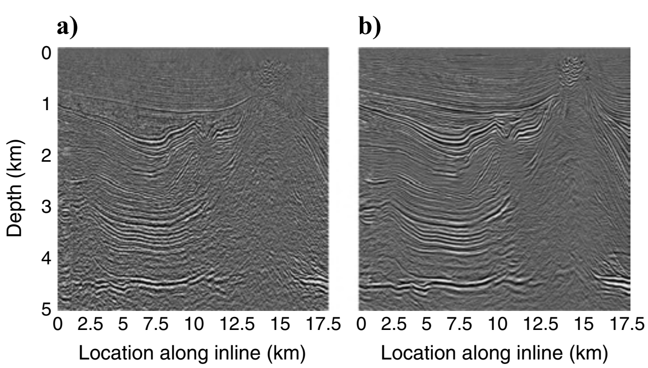

Figure 13. Depth migrated section from a 3D land-marine transition area, northwest Germany. (a) Directional angle decomposition followed by normal (no weighting) stack. (b) Image in the same area with specular energy weighted stack applied.

Example D

Figure 16 shows two depth slices from a fractured carbonate reservoir in the North Sea. Figure 16a demonstrates the resolution that can be obtained using directional angle decomposition followed by normal stack. Figure 16b shows a high-resolution image of the same reservoir, emphasizing the fracture system and the channels, that were obtained by using a diffraction energy weighted stack (as opposed to the specular energy weighted stack shown in the previous examples),

$$I_{\mathrm{diff}}(\mathbf{M}) = \sum_{\nu_1,\nu_2} I_\nu(\mathbf{M},\nu_1,\nu_2) \cdot f^p_{\mathrm{diff}}(\mathbf{M},\nu_1,\nu_2), \tag{25}$$

where

$$f_{\mathrm{diff}}(\mathbf{M},\nu_1,\nu_2) = 1 - f_{\mathrm{spec}}(\mathbf{M},\nu_1,\nu_2) \tag{26}$$

is an operator that decays the specular energy.

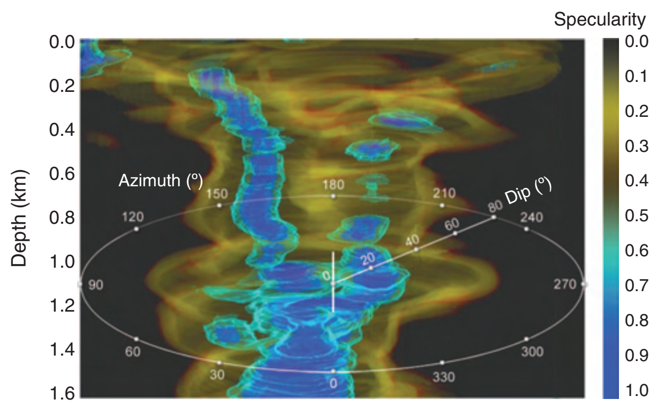

Figure 14. Specularity directional angle gather along pinchout: Two different specular directions at the same depth level.

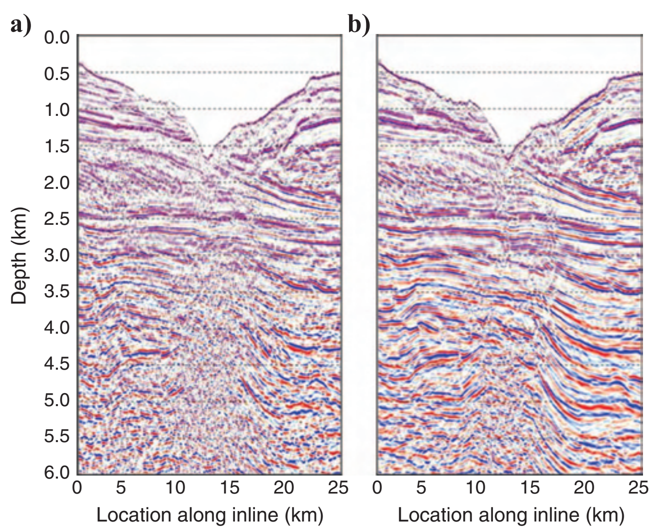

Figure 15. Imaging a "hidden" structure in offshore Australia. (a) Directional angle decomposition followed by normal stack. (b) Image in the same area with specular energy weighted stack applied.

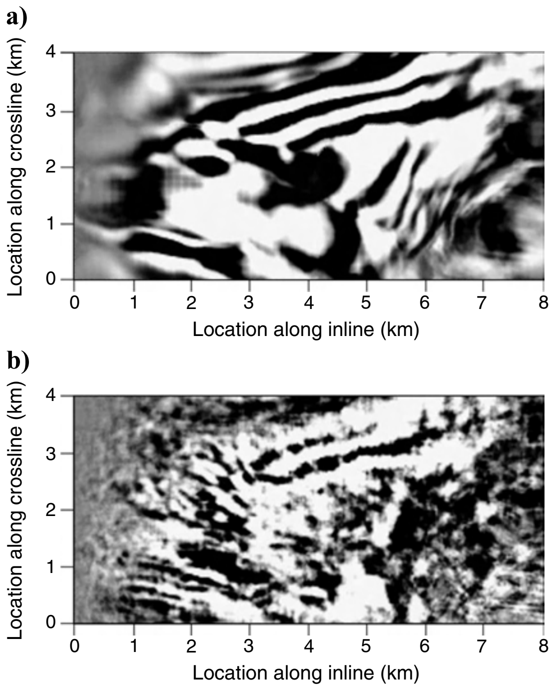

Figure 16. Two depth slices from a fractured carbonate reservoir in the North Sea. (a) Image obtained using directional angle decomposition followed by normal stack. (b) Image with high-resolution features obtained using diffraction energy weighted stack.

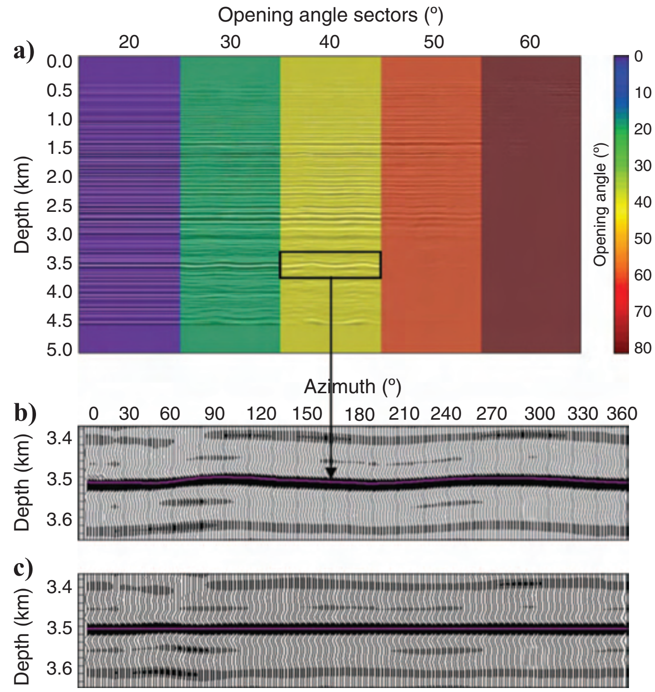

Figure 19. Full-azimuth reflection-angle event. (a) Five extracted opening angle sectors (20°, 30°, 40°, 50°, and 60°), each displaying full-azimuth reflections. The azimuthally varying reflector, marked by a rectangle, indicates an azimuthal anisotropy effect. (b) The reflector is magnified and overlain by automatic RMO picks. (c) RMO picks are used to flatten the event.

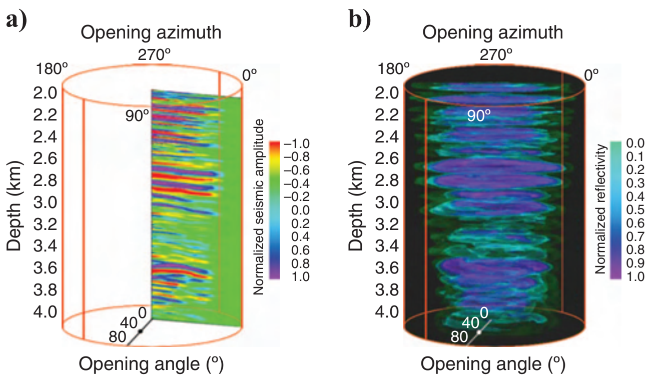

Figure 17. 3D cylindrical reflection-angle gather. (a) Selected azimuthal sector. (b) Full 3D volume with transparency mode, emphasizing the high reflectivity values.

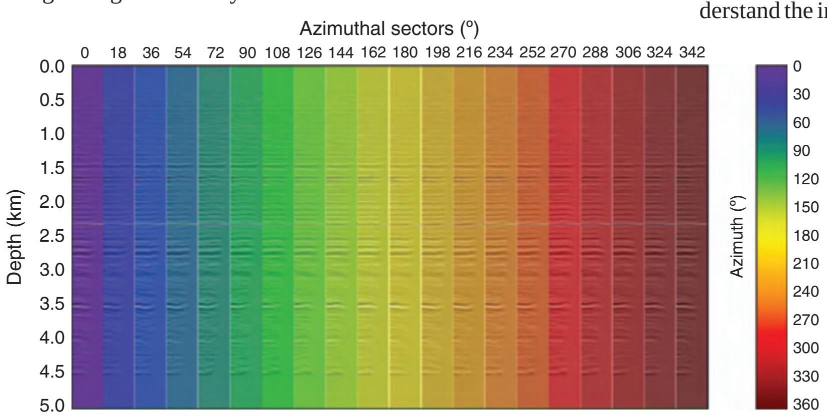

Figure 18. Twenty azimuthal sectors of reflection-angle gathers interactively extracted from the 3D cylindrical gather. Residual moveout curves vary with azimuths, indicating azimuthal anisotropy effect.

Full-azimuth reflection-angle gathers were created using equation 5. An example of a 3D reflection-angle gather in this area is shown in Figure 17. It is displayed as a cylinder (Figure 17a) and with transparency (Figure 17b), so that the full dimensionality of the amplitude versus opening angle and opening azimuth can be studied. These full-azimuth image gathers can provide diagnostic quality control regarding the accuracy of the velocity models, and enable the automatic detection of residual moveout (RMO) errors. The gathers also can be sampled in full-angle or full-azimuth sectors to better understand the influence of azimuth on the velocity model, and to better understand the behavior of seismic amplitude as a function of opening angle and azimuth. Figure 18 shows 20 azimuthal sectors of reflection-angle gathers that were extracted on the fly from the cylindrical gather shown in Figure 17. Figure 19a shows five extracted opening angle sectors (20°, 30°, 40°, 50°, and 60°), each of which displays full-azimuth reflections.

The azimuthally varying reflector indicates an azimuthal anisotropic effect, and is marked by a rectangle. In Figure 19b, the reflector is magnified and overlain by automatic RMO picks, which are used to flatten the event (Figure 19c). Although azimuthally varying reflectors can result from lateral heterogeneity, in this example the target area is known to be a fractured carbonate reservoir with many external supported indications, e.g., vertical seismic profiling (VSP) information and S-waves.

CONCLUSIONS

This paper presents a novel imaging system for generating continuous, full-azimuth, angle-domain image gathers. The set of four angles within the local angle domain is introduced. Forward and inverse transforms between the LAD and the directions of incident and reflected rays are described. Although the method is presented as a ray-based imaging approach, the theory is valid for wave equation imaging as well. Two complementary angle gathers, directional and reflection, deliver high-resolution information about the subsurface model. In particular, the new directional image gathers allow the automatic extraction of geometrical attributes, such as dip, azimuth and specularity/continuity, and enable the generation of different types of images by weighting either specular or diffraction energy.

It has been shown that several specular directions might coexist at the same image point, associated with conflicting dips (unconformities and pinchouts). Continuous structure surfaces and discontinuous subscale small objects, such as channels and fractures, can be detected, even below complex geological structures. Full-azimuth reflection-angle gathers provide information about full-azimuth residual moveouts, and therefore measure the accuracy of the background velocity model from all angles and azimuths. In particular, the full-azimuth RMO can be used as indicators of the existence of azimuthal anisotropy effects due to fractures. In addition, the true amplitude, full-azimuth reflection-angle gathers serve as optimal data for amplitude analysis (AVAZ), and for the extraction of high-resolution elastic properties.

The full-azimuth angle-domain decomposition performed independently for every image point enables control and customization of the locality, direction, and scope of the area being studied, and the corresponding seismic data. The system, therefore, might be used locally as a target-oriented system for direct, high-resolution reservoir imaging, as well as globally for full-volume imaging of massive amounts of data.

ACKNOWLEDGMENTS

We thank Allon Bartana, Edip Baysal, Anat Canning, David Chase, Duane Dopkin, Adam Farris, Ofra Kalechshtain, Dan Kosloff, Evgeny Kozlov, Ronit Levy, Beth Orshalimy, Evgeny Ragoza, S.P. Singh, and many other colleagues at Paradigm for their contribution to the development work leading to this paper. We are grateful to Norman Bleistein for the valuable discussions, and to the Geophysics editors and reviewers Jose Carcione, Ivan Vasconcelos, Stig-Kyrre Foss and Samuel Gray for their many valuable comments and suggestions, which helped to improve the content and style of this paper. We would also like to thank RWE-Dea and our other customers for their collaboration and permission to use their data in this study.

REFERENCES

Audebert, F., P. Froidevaux, H. Rakotoarisoa, and J. Svay-Lucas, 2002, Insights into migration in the angle domain: 72nd Annual International Meeting, SEG, Expanded Abstracts, 1188–1191.

Bansal, R., and M. G. Imhof, 2005, Diffraction enhancement in prestack seismic data: Geophysics, **70**, no. 3, V73–V79, doi: 10.1190/1.1926577.

Beylkin, G., 1985, Imaging of discontinuities in the inverse scattering problem by inversion of a casual generalized Radon transform: Journal of Mathematical Physics, **26**, 99–108, doi: 10.1063/1.526755.

Beylkin, G., and R. Burridge, 1990, Linearized inverse scattering problems in acoustics and elasticity: Wave Motion, **12**, 15–52, doi: 10.1016/0165-2125(90)90017-X.

Biondi B., 2007a, Angle-domain common-image gathers from anisotropic migration: Geophysics, **72**, no. 2, S81–S91, doi: 10.1190/1.2430561.

Biondi, B., 2007b, Residual moveout in anisotropic angle-domain common-image gathers: Geophysics, **72**, no. 2, S93–S103, doi: 10.1190/1.2430562.

Bleistein, N., 1987, On the imaging of reflectors in the earth: Geophysics, **52**, 931–942, doi: 10.1190/1.1442363.

Bleistein, N., J. K. Cohen, and J. W. Stockwell Jr., 2001, Mathematics of multidimensional seismic imaging, migration, and inversion: Springer.

Bleistein, N., and S. H. Gray, 2002, A proposal for common-opening-angle migration/inversion: Center for Wave Phenomena, Colorado School of Mines, Research Report CWP-420.

Bleistein, N., Y. Zhang, S. Xu, G. Zhang, and S. H. Gray, 2005a, Kirchhoff inversion in image point coordinates recast as source/receiver point processing: 75th Annual International Meeting, SEG, Expanded Abstracts, 1697–1700.

Bleistein, N., Y. Zhang, S. Xu, G. Zhang, and S. H. Gray, 2005b, Migration/inversion: think image point coordinates, process in acquisition surface coordinates: Inverse Problems, **21**, 1715–1744, doi: 10.1088/0266-5611/21/5/013.

Brandsberg-Dahl, S., M. V. de Hoop, and B. Ursin, 2003, Focusing in dip and AVA compensation on scattering-angle/azimuth common image gathers: Geophysics, **68**, 232–254, doi: 10.1190/1.1543210.

Brandsberg-Dahl, S., M. V. de Hoop, and B. Ursin, 1999, Velocity analysis in the common scattering-angle/azimuth domain: 69th Annual International Meeting, SEG, Expanded Abstracts, 1715–1718.

de Hoop, M. V., and N. Bleistein, 1997, Generalized Radon transform inversions for reflectivity in anisotropic elastic media: Inverse Problems, **13**, 669–690, doi: 10.1088/0266-5611/13/3/009.

de Hoop, M. V., and C. Spencer, 1996, Quasi-Monte Carlo integration over $S^2 \times S^2$ for migration $\times$ inversion: Inverse Problems, **12**, 219–239.

de Hoop, M. V., C. Spencer, and R. Burridge, 1999, The resolving power of seismic amplitude data: An anisotropic inversion/migration approach: Geophysics, **64**, 852–873, doi: 10.1190/1.1444595.

de Vries, P., D. V. van Coevorden, and A. Lagendijk, 1998, Point scatterers for classical waves: Reviews of Modern Physics, **70**, 447–466, doi: 10.1103/RevModPhys.70.447.

Fomel, S., E. Landa, and M. T. Taner, 2006, Post-stack velocity analysis by separation and imaging of seismic diffractions: 76th Annual International Meeting, SEG, Expanded Abstracts, 2559–2563a.

Foss, S.-K., and B. Ursin, 2004, 2.5-D modeling, inversion and angle-migration in anisotropic elastic media: Geophysical Prospecting, **52**, 65–84, doi: 10.1046/j.1365-2478.2004.00400.x.

Goldin, S., 1992, Estimation of reflection coefficient under migration of converted and monotype waves: Soviet Geology and Geophysics, **33**, 76–90.

Gray, S. H., and N. Bleistein, 2009, True-amplitude Gaussian-beam migration: Geophysics, **74**, no. 2, S11–S23, doi: 10.1190/1.3052116.

Gray, S. H., Y. Xie, C. Notfors, T. Zhu, D. Wang, and C.-O. Ting, 2009, Taking apart beam migration: The Leading Edge, **28**, 1098–1108, doi: 10.1190/1.3236380.

Hill, N. R., 2001, Prestack Gaussian-beam depth migration: Geophysics, **66**, 1240–1250, doi: 10.1190/1.1487071.

Hubral, P., J. Schleicher, and M. Tygel, 1996, A unified approach to 3-D seismic reflection imaging, Part I: Basic concepts: Geophysics, **61**, 742–758, doi: 10.1190/1.1444001.

Khaidukov, V., E. Landa, and T. J. Moser, 2004, Diffraction imaging by focusing-defocusing: An outlook on seismic superresolution: Geophysics, **69**, 1478–1490, , doi: 10.1190/1.1836821.

Koren, Z., I. Ravve, A. Bartana, and D. Kosloff, 2007, Local angle domain in seismic imaging: 69th Conference and Exhibition, EAGE, Extended Abstracts, P287.

Koren, Z., I. Ravve, and R. Levy, 2010, Specular-diffraction imaging from directional angle decomposition: 72nd Conference and Exhibition, EAGE, Extended Abstracts, G045.

Koren, Z., I. Ravve, E. Ragoza, A. Bartana, and D. Kosloff, 2008, Full-azimuth angle domain imaging: 78th Annual International Meeting, SEG, Expanded Abstracts, 2221–2225.

Koren, Z., X. Sheng, and D. Kosloff, 2002, Target-oriented common reflection angle migration: 72nd Annual International Meeting, SEG, Expanded Abstracts, 1196–1199.

Kozlov, E., N. Barasky, E. Korolev, A. Antonenko, and E. Koshchuk, 2004, Imaging scattering objects masked by specular reflections: 74th Annual International Meeting, SEG, Expanded Abstracts, 1131–1134.

Kozlov, E. A., Z. Koren, D. N. Tverdohlebov, and A. N. Badeikin, 2009, Corner reflectors — a new concept of imaging vertical boundaries: 71st Conference and Exhibition, EAGE, Extended Abstracts, Z039.

Miller, D., M. Oristaglio, and G. Beylkin, 1987, A new slant on seismic imag-

ing: Migration and integral geometry: Geophysics, **52**, 943–964, doi: 10.1190/1.1442364.
Mozer, T. J., and C. B. Howard, 2008, Diffraction imaging in depth: Geophysical Prospecting, **56**, 627–641, doi: 10.1111/j.1365-2478.2007.00718.x.
Nolan, C., and W. Symes, 1996, Imaging in complex velocities with general acquisition geometry: TRIP, the Rice Inversion Project, Rice University, technical report.
Reshef, M., N. Lipzer, and E. Landa, 2009, Interval velocity analysis in complex areas — azimuth considerations: 71st Conference and Exhibition, EAGE, Extended Abstracts, U010.
Rickett, J. E., and P. C. Sava, 2002, Offset and angle-domain common image-point gathers for shot-profile migration: Geophysics, **67**, 883–889, doi: 10.1190/1.1484531.
Rousseau, V., L. Nicoletis, J. Svay-Lucas, and H. Rakotoarisoa, 2000, 3D true amplitude migration by regularisation in angle domain: 62nd Conference and Exhibition, EAGE, Extended Abstracts, B-13.
Schleicher, J., M. Tygel, and P. Hubral, 2007, Seismic true-amplitude imaging: SEG Geophysical Developments Series No. 12.
Schleicher, J., M. Tygel, and P. Hubral, 1993, 3-D true-amplitude finite-offset migration: Geophysics, **58**, 1112–1126, doi: 10.1190/1.1443495.
Sherwood, J. W. C., K. Sherwood, H. Tieman, and K. Schleicher, 2009, 3D beam prestack depth migration with examples from around the world: The Leading Edge, **28**, 1120–1127, doi: 10.1190/1.3236382.
Shtivelman, V., and S. Keydar, 2005, Imaging shallow subsurface inhomogeneities by 3D multipath diffraction summation: First Break, **23**, 39–42.
Sollid, A., and B. Ursin, 2003, Scattering-angle migration of ocean-bottom seismic data in weakly anisotropic media: Geophysics, **68**, 641–655, doi: 10.1190/1.1567234.
Soubaras, R., 2003, Angle gathers for shot-record migration by local harmonic decomposition: 73rd Annual International Meeting, SEG, Expanded Abstracts, 889–892.
Taner, M. T., S. Fomel, and E. Landa, 2006, Separation and imaging of seismic diffractions using plane-wave decomposition: 76th Annual International Meeting, SEG, Expanded Abstracts, 2401–2405.
ten Kroode, A. P. E., D. J. Smit, and A. R. Verdel, 1994, Linearized inverse scattering in the presence of caustic: SPIE — The International Society for Optical Engineering, Expanded Abstracts, 28–42.
Tygel, M., J. Schleicher, and P. Hubral, 1996, A unified approach to 3-D seismic reflection imaging, part II: Theory: Geophysics, **61**, 759–775, doi: 10.1190/1.1444002.
Wapenaar, K., E. Slob, and R. Snieder, 2010, On seismic interferometry, the generalized optical theorem, and the scattering matrix of a point scatterer: Geophysics, **75**, no. 3, SA27–SA35, doi: 10.1190/1.3374359.
Wu, R.-S., and L. Chen, 2006, Directional illumination analysis using beamlet decomposition and propagation: Geophysics, **71**, no. 4, S147–S159, doi: 10.1190/1.2204963.
Xu, S., H. Chauris, G. Lambaré, and M. Noble, 2001, Common-angle migration: A strategy for imaging complex media: Geophysics, **66**, 1877–1894, doi: 10.1190/1.1487131.